Corrosion Science 158 (2019) 108078

Contents lists available at ScienceDirect

Corrosion Science

journal homepage: www.elsevier.com/locate/corsci

Effect of $CaCO_3$-saturated solution on CO_2 corrosion of mild steel explored in a system with controlled water chemistry and well-defined mass transfer conditions

H. Mansoori*, D. Young, B. Brown, S. Nesic, M. Singer

Institute for Corrosion and Multiphase Technology, Department of Chemical & Biomolecular Engineering, Ohio University, 342 West State Street, Athens, OH, 45701, USA

ARTICLE INFO

Keywords:
CO_2 corrosion
Corrosion product
Fe_3C
$CaCO_3$
Isostructurality
Iron-calcium carbonate

ABSTRACT

The effect of Ca^{2+} on the corrosion product layers when the CO_2-containing electrolyte is saturated with respect to $CaCO_3$, as frequently observed in oil production systems, was studied by weight loss, electrochemical techniques, and surface characterizations. An improved experimental set up was used and all experimental parameters reported. Results show that precipitation of corrosion products in solutions with or without $CaCO_3$ was due to the favorable water chemistry obtained at the steel surface compared to the bulk solution. The presence of Ca^{2+} did not jeopardize the final protectiveness of corrosion product layer, but seemed to delay its growth.

1. Introduction

In oil and gas production, CO_2 corrosion and scaling (i.e. formation of $CaCO_3$, $MgCO_3$, etc.) happen simultaneously. Distinct bodies of research have been conducted to address scaling and corrosion issues in the past. However, there is minimal information in the literature relating to situations where corrosion and scaling are considered together, despite there being indications that heavy scaling may lead to localized attack and loss of integrity [1]. Consequently, there is a need to explore potential relationships between scaling and corrosion and their effect on the deterioration of mild steel.

Brine, co-produced along with a hydrocarbon phase in oil and gas wells, is an aqueous phase containing a variety of dissolved species [2–4]. Sodium (Na^+), chloride (Cl^-), and calcium (Ca^{2+}) ions are usually present in these brines at higher concentrations than other ions. All oil and gas wells contain some amount of CO_2 and, under the right conditions, calcium carbonate ($CaCO_3$) will readily precipitate if its solubility limit is exceeded due to its fast precipitation kinetics [5]. Indeed, the brine usually contains a considerable amount of CO_2 [6] and this results in CO_2 corrosion of mild steels, also known as “sweet corrosion”, by far the most common type of corrosion encountered in the upstream oil and gas industry [7].

Iron carbonate ($FeCO_3$) is the main corrosion product in CO_2 corrosion. $FeCO_3$ is here referred to as a “corrosion product”, rather than “scale” (a term often used in the literature), since its constituent cation (Fe^{2+}) comes from the corroding steel surface. This is done to distinguish it from, for example, $CaCO_3$, which is referred to as a “scale” as its constituent cation (Ca^{2+}) comes from the bulk solution and is then deposited on the steel surface [8]. An $FeCO_3$ layer can limit corrosion of steel by acting as a diffusion barrier for species involved in cathodic and anodic reactions and by reducing the active surface area of the steel, both of which will decrease the rate of the iron dissolution (anodic) reaction. However, partial dissolution and/or destruction of this protective layer can lead to localized corrosion [9]. The term “protective layer” is used herein to describe a metal carbonate layer precipitated on a steel surface which can decrease corrosion rates to an acceptable level, which is typically below 0.1 mm/yr. It is noteworthy that in CO_2 corrosion passivation of mild steel will not occur due to the acidic conditions, so there will always be some residual corrosion occurring beneath the porous protective layers that form.

Most laboratory corrosion studies have been performed in various dilute aqueous NaCl electrolytes,[1] while, in reality, Ca^{2+} ions are also present in produced brines [10]. The solid $CaCO_3$ (calcite) and $FeCO_3$ (siderite) are isostructural with a hexagonal unit cell. This would indicate that their constituent cations (Ca^{2+} and Fe^{2+}) can coexist in a substitutional solid solution as a mixed metal carbonate, with a chemical formula designated as $Ca_xFe_{1-x}CO_3$ ($0 \le x \le 1$). However, the solubility of $CaCO_3$ is about two orders of magnitude greater than $FeCO_3$. Therefore, substitution of Fe^{2+} by Ca^{2+} in the lattice of $FeCO_3$ can be hypothesized to alter the solubility of the mixed metal carbonate

* Corresponding author.
E-mail address: hm419213@ohio.edu (H. Mansoori).

[1] Terms “electrolyte” and “solution” are used interchangeably within this manuscript.

https://doi.org/10.1016/j.corsci.2019.07.004
Received 30 November 2018; Received in revised form 25 April 2019; Accepted 2 July 2019
Available online 09 July 2019
0010-938X/

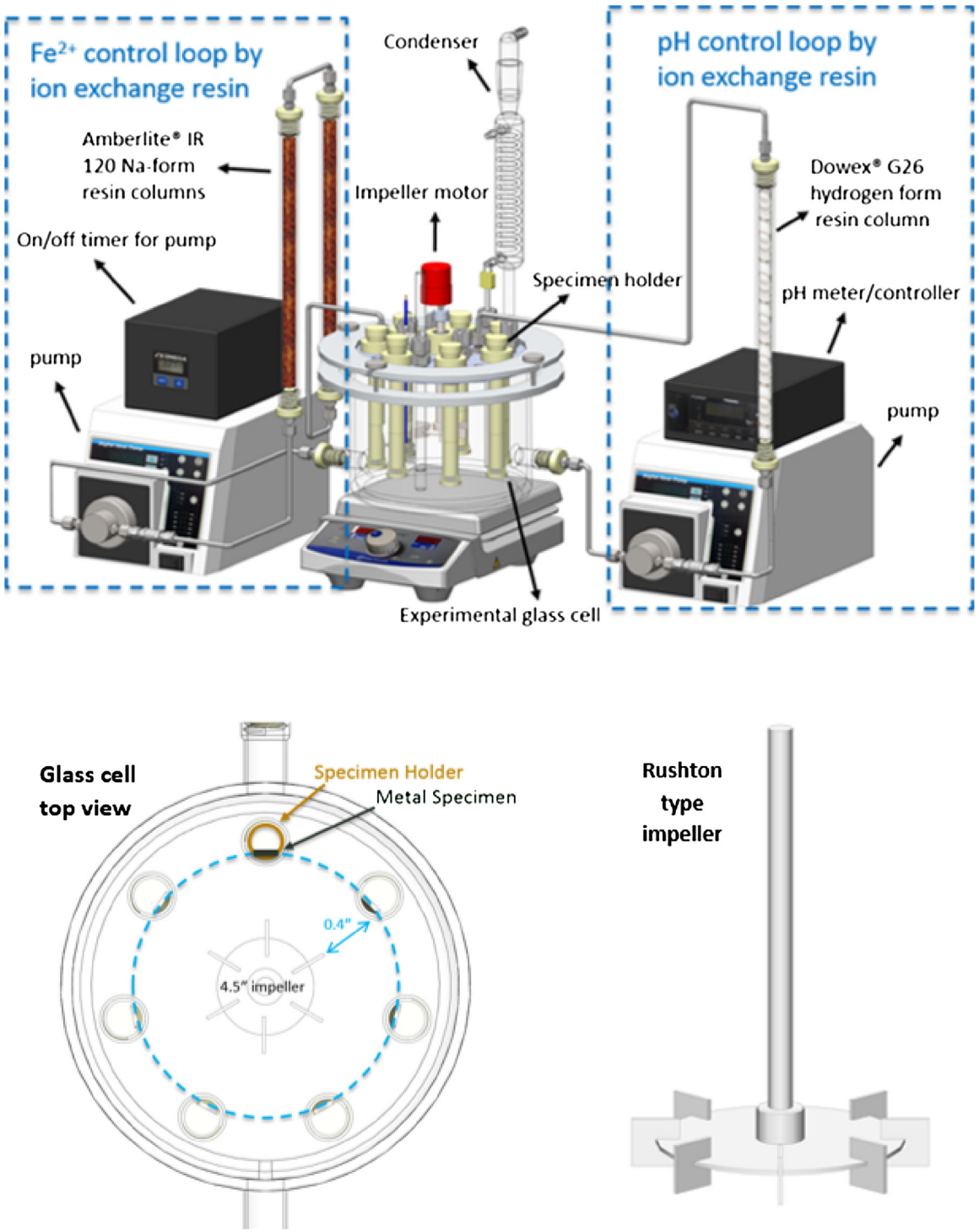

Fig. 1. Schematic view of the system equipped with impeller and $[Fe^{2+}]/[H^{+}]$ control loops. The impeller diameter was 4.5″, the distance between the impeller blades and the specimen surface was 0.4″, and the glass cell had an 8″ internal diameter. (All drawings courtesy of Cody Shafer, OU ICMT).

layers in comparison with pure $FeCO_3$ layers, due to compositional heterogeneity, so that morphological alterations can be expected [11].

There are few research studies in the literature that address the effect of Ca^{2+} ions on CO_2 corrosion [8]. The results of such studies are often contradictory and the corrosion mechanisms in the presence of alkaline earth cations, such as Ca^{2+}, have not been methodically characterized. There are studies claiming that the general corrosion rate is higher in the presence of calcium ions [12,13]. Conversely, some researchers came up with the exact opposite conclusions [14–16]. There are claims that Ca^{2+} ions initiate pitting corrosion attack [11,16]; while another research study states that the presence of Ca^{2+} ions could postpone the occurrence of pitting on mild steel [17]. Such discrepancies concerning the true effect of Ca^{2+} on CO_2 corrosion are often due to inadequate experimental procedures and setups which did not enable proper control of the solution chemistry. This confusion found in the open literature prompted the development of different procedures and construction of a new experimental setup for elucidating the relevant issues surrounding CO_2 corrosion in the presence of Ca^{2+} ions.

Obviously, water speciation is one of the most influential

parameters that governs both processes: scaling and corrosion. The saturation degree of $CaCO_3$ and $FeCO_3$ in solution is a parameter even more important than the individual ion concentrations when studying the effect of Ca^{2+} ions in CO_2 corrosion. The precipitation kinetics of solid $CaCO_3$ and $FeCO_3$ are greatly influenced by the bulk saturation degree which acts as the main driving force [18–20]. Researchers often overlooked this important environmental parameter, exclusively relying on ion concentrations as the core influencing parameter [13,16,21]. In the calculation of carbonate saturation in the bulk solution, the activity of the relevant ions (e.g., Ca^{2+}, CO_3^{2-}) plays a crucial role. Activity is referred to as the effective concentration of an ion in a non-ideal solution. For ideal solutions, the activity of ions is equal to its concentration. However, in the case of a non-ideal solution, the activity of a particular ion can be much lower or higher than its concentration [22]. Therefore, ignoring the non-ideality of the solution can lead to miscalculations of $CaCO_3$ and $FeCO_3$ saturation degrees. This is especially true for studies focused on corrosion/scale interactions, where authors typically do not take non-ideality into consideration and consequently report incorrect values for the carbonates saturation degree [11,12]. pH is another key parameter which has a considerable effect on the corrosion rates and the precipitation rates of $CaCO_3$ and $FeCO_3$. Many studies published on the effect of Ca^{2+} on CO_2 corrosion describe experiments where the initial and final solution pHs are not the same due to change of water chemistry over the course of long-term experiments [12,14,16]. In some cases, pH is not reported at all [13,21].

The corrosion behavior and the formation of corrosion product layers and scales are also influenced by mass transfer of the relevant ions from/to the bulk solution and through surface layers [23]. Mass transfer rate influences the concentration of the aqueous species near the corroding metal surface where metal carbonates form. Consequently, the morphology and other properties of the surface layers can be considerably affected by mass transfer characteristics. Experimental data generated by a setup with undefined mass transfer characteristics is very difficult to reproduce by other researchers.

In the current research effort, an attempt was made to overcome the reported experimental difficulties and to obtain more reliable and repeatable results when studying the influence of Ca^{2+} on the mild steel CO_2 corrosion mechanisms. The results below were obtained in a system where the water chemistry of the system was tightly controlled over the course of the experiments and mass transfer conditions in the experimental setup were well-defined.

2. Experimental setup and methodology

2.1. Controlled water chemistry glass cell setup

As mentioned in the introduction, the discrepancies seen in the literature regarding the true effect of Ca^{2+} on CO_2 corrosion are in part due to poorly controlled water chemistry, unknown bulk saturation degree of metal carbonates, and poorly defined mass transfer conditions. Therefore, in the present study, the aforementioned issues were overcome by using an improved glass cell setup.

In the newly designed glass cell, seven mild steel specimens, identical in size (1.5 cm^2 x 1.5 cm^2), were held in place using cylindrical PEEK rods as specimen holders (Fig. 1). One of the specimen holders was specially built to have a specimen with an electrical connection while the other holders held specimen for weight loss and cross-section surface analysis. All seven steel specimens experienced identical flow (i.e. the same shear stress and mass transfer conditions) as they were all located at the same radial distance from the center of the glass cell (Fig. 1). An impeller was used to create uniform mass transfer and shear stress across the specimen surfaces. This was an advancement introduced to eliminate the non-uniformity of flow and mass transfer experienced by the unstable hanging specimens in the conventional glass cell setup used in a previous study relating to this topic [12]. Although, in the current study, the solution to surface area ratio is almost 5 times larger than recommended [24], the increased concentration of ferrous ions released by the seven specimens corroding in 3-liters of solution was addressed by the new cell design as described below.

Specific modifications were made to control the water chemistry of the system (pH, $[Fe^{2+}]$, $[Ca^{2+}]$). The partial pressure of CO_2 maintained by a continuous sparging of CO_2 into solution and the temperature was controlled by using a hot plate with thermocouple feedback. The pH and $[Fe^{2+}]$ were controlled by using H-form and Na-form ion-exchange resins installed in two independent control loops attached to the main glass cell. Both types of ion exchange resin interchange ions by accepting cations from the solution and releasing either protons (from the H-form resin) or sodium ions (from the Na-form resin) back to the solution to maintain a charge balance. To maintain the $[Fe^{2+}]$, a sample of the solution was collected and externally measured twice daily with a spectrophotometer (Thermo Scientific GENESIS 10 Vis) using phenanthroline as the reagent [25]. When the measured $[Fe^{2+}]$ reached or exceeded the target value (~10 ppm in this study), the pump moving the solution through the Na-form ion-exchange column was manually turned on to decrease the $[Fe^{2+}]$. An on/off timer was used to control the amount of time the pump would move the solution through the Na-form ion-exchange resin. The pH of the solution was maintained automatically by using a pH controller to turn on or turn off the positive displacement pump moving the solution through the H-form ion-exchange column. For more explanation about the efficiency of ion-exchange resins and their functions in corrosion studies, please refer to a recent publication by Zhong et al. [26].

The test solution was kept saturated with respect to calcium carbonate over the course of 7-day experiments, corresponding to a stable $[Ca^{2+}]$ of approximately 160 ppm, by maintaining a layer of solid calcium carbonate at the bottom of the glass cell. The $[Ca^{2+}]$ was measured at the beginning and end of experiments using an Inductively Coupled Plasma (ICP) technique. The results were in agreement with concentration values calculated using Geochemist Work Bench software (using PHREEQC as the thermodynamic database) considering the non-ideality of the solution.

2.2. Mass transfer characterization of the glass cell with impeller

Defining the hydrodynamic and mass transfer conditions of any new experimental corrosion setup is essential when studying the influence of flow on corrosion, and helps ensure reproducibly of the results [27]. A ferri-ferrocyanide aqueous solution is typically employed to define the mass transfer conditions for various flow geometries and related hydrodynamics [28]. In the current experimental setup, the ferri-ferrocyanide coupled electrochemical reactions, Eq. (1), were used to measure the limiting currents and, thus, define the mass transfer coefficient.

$$Fe(CN)_6^{3-} + e^- \leftrightharpoons Fe(CN)_6^{4-} \quad (1)$$

Table 1 shows the experimental conditions for the mass transfer characterization experiments. Measurements were conducted at 40 °C and 50 °C to prove repeatability. Rotational speeds for measurements at each temperature ranged from 50 rpm to 200 rpm. Fig. 2 depicts an example of limiting currents obtained at 50 °C at each rotational speed. The dependence of the Sherwood (Sh) number on the Reynolds (Re) and Schmidt (Sc) numbers was defined by performing multiple regression to calculate the unknown constants pertaining to the specific geometry of the glass cell setup with this impeller. The final coefficients are shown in Eq. (2).

$$Sh = 1.47\, Re^{0.63} Sc^{0.33} \quad (2)$$

The exponent for Sc number in Eq. (2) was set at 0.33 following the original correlation for a single-phase pipe geometry proposed by Berger and Hau (Eq. (3)) [29]. This exponent was not part of the regression analysis since the Sc number varied only very slightly over the experimental conditions tested.

Table 1
Experimental condition for mass transfer characterization.

Parameter	Description
Material	Nickel (Ni) Flat Square Specimen (A = 1.58 cm^2)
Temperature	40 °C, 50 °C
Total Pressure (N_2 as completing gas)	1 bar
Reference Electrode	Saturated Ag/AgCl
Electrolyte	0.5 M NaOH 0.01 M of $K_3Fe(CN)_6$ 0.01 M of $K_4Fe(CN)_6.3H_2O$
Rotational Speed Range	50, 100, 150 rpm
Electrochemical Technique	Potentiodynamic Sweep 0.4 V above (anodic) and 1 V below (cathodic) OCP 5 mV/s Polarization Scan Rate
Dissolved O_2	< 5 ppb

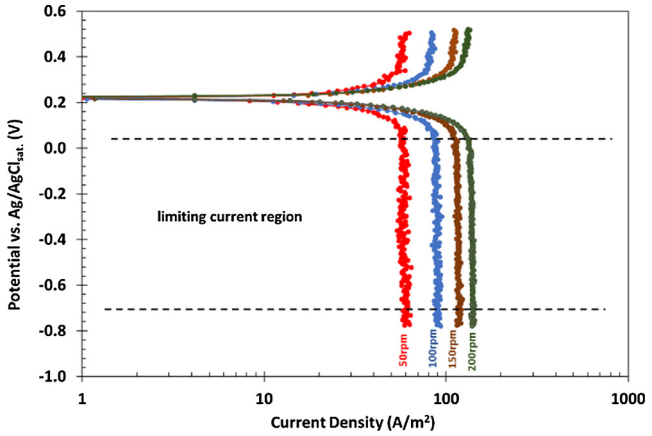

Fig. 2. Limiting currents obtained at 50 °C and varying rotational speeds using ferri-ferrocyanide coupled reactions.

$$Sh = 0.0165\, Re^{0.86} Sc^{0.33} \quad (3)$$

With the goal of relating the conditions in this glass cell with single-phase pipe flow conditions in the field, the equivalent fluid velocity in a pipe corresponding to selected rotational speed of the impeller in the glass cell setup can be determined by equating the mass transfer coefficients in the pipe and the glass cell (Eq. (4)).

$$V = (89.1 \times N^{0.63} \times d_{pipe}^{0.14} \times d_{imp.}^{0.26} \times \upsilon^{0.23})^{1.163} \quad (4)$$

where:

N = revolution/sec of impeller
d_{pipe} = diameter of pipe (m)
$d_{imp.}$ = diameter of impeller (m)
υ = kinematic viscosity (m^2/s)

Fig. 3 shows the almost linear relationship between the flow velocity in a 0.1 m ID pipe (a typical pipe internal diameter) and the rotational speed in the glass cell with impeller, based on Eq. (4). The actual impeller speed used in the current experiments (20 rpm) corresponds to approximately 0.5 m/s in a pipe flow, which is a reasonable condition to simulate.

2.3. Methodology used in corrosion experiments

Two series of corrosion experiments were performed (and repeated), one without Ca^{2+} ions (as a baseline) and one in a $CaCO_3$ saturated solution (with approximately 160 ppm Ca^{2+}). Other than that, both tests were conducted under the same experimental conditions as described in Table 2. The experiments were conducted at atmospheric pressure at 80 °C and 0.53 bar pCO_2. After addition of 1 wt% NaCl (to both electrolytes), $CaCO_3$ reagent (to the electrolyte containing Ca^{2+}), or $NaHCO_3$ (to the baseline electrolyte), the electrolytes were deoxygenated by sparging with CO_2 for at least two hours prior to each experiment as they were heated to 80 °C. At 80 °C, the water vapor pressure is 0.47 bar with the balance gas being CO_2. In these conditions, the autogenous initial pH for the electrolyte with the presence of $CaCO_3$ reagent, when the system was in equilibrium, was pH 6.2. Therefore, to have similar testing environments, the pH of the baseline electrolyte was initially adjusted to 6.2 (using $NaHCO_3$). CO_2 gas was continuously bubbled into the solutions to maintain saturation with CO_2 during corrosion experiments. The pH was maintained at 6.2 ± 0.1 by the means of H-form ion-exchange resin (Dowex® G26). The [Fe^{2+}] was controlled to be not greater than 10 ppm using Na-form ion-exchange resin (Amberlite® IR 120). The $CaCO_3$-saturated solution initially contained 1.2 g/L powder $CaCO_3$ reagent with 99% purity (ACROS Organics™). This excess amount of $CaCO_3$ in the solution was calculated to be three times higher than what was needed in order for the solution to remain saturated with respect to $CaCO_3$ over the course of the long-term experiments. The excess $CaCO_3$ reagent guaranteed that the solution remained saturated with respect to $CaCO_3$ with a stable [Ca^{2+}] due to the relatively fast kinetics of $CaCO_3$ precipitation/dissolution [20].

The specimens were made of UNS G10180[2] that has a ferritic-pearlitic microstructure with a chemical composition described Table 3. The electrochemical and weight loss specimens were wet-polished with silicon carbide papers up to 600 grit. Following the polishing process, the specimens were rinsed with isopropanol and placed in an ultrasonic cleaner for 2 min to remove any possible debris from the steel surface. Finally, they were dried by cold air and weighed prior to immersion into the test solutions. A three-electrode system, including working, counter, and reference electrodes along with a Gamry Reference600™ potentiostat, was used to conduct electrochemical measurements. The corrosion rate was measured at least twice per day using linear polarization resistance (LPR) method and open circuit potential (OCP) was also recorded. The duration of each experiment was seven days. Two specimens were retrieved from the glass cell at day 2, 4, and 7 from each experiment to obtain the weight loss (WL) and conduct surface characterizations using techniques including scanning electron microscopy (SEM), energy dispersive X-ray spectroscopy (EDS), and X-ray diffraction (XRD).

$FeCO_3$ saturation degree (S_{FeCO_3}) is an important parameter in CO_2 corrosion studies, influencing precipitation rate of $FeCO_3$ and thus the corrosion mechanism [30,31]. The S_{FeCO_3} value was calculated over time for experiments with and without Ca^{2+} using the following equation:

$$S_{FeCO_3} = \frac{C_{Fe^{2+}} \bullet C_{CO_3^{2-}}}{K_{sp,\,FeCO_3}} \quad (6)$$

where $C_{Fe^{2+}}$ and $C_{CO_3^{2-}}$ are ferrous ion (Fe^{2+}) and carbonate ion (CO_3^{2-}) concentrations in the bulk solution. For each [Fe^{2+}] measured, the current temperature and pH were used to calculate [CO_3^{2-}] from an equilibrium model for CO_2 speciation in aqueous environments [32]. The $K_{sp,\,FeCO_3}$ in Eq. (6) is the solubility product of $FeCO_3$ calculated using an equation proposed by Sun, et al. [33]:

$$logK_{SP,\,FeCO_3} = -59.3498 - 0.041377 \bullet T_k - \frac{2.1963}{T_k} + 24.5724 \bullet Log(T_k) + 2.518 \bullet I^{0.5} - 0.657 \bullet I \quad (7)$$

where T_k is the temperature (in Kelvin) and I is the ionic strength. Eq. (7) was developed to take into account the non-ideality of the solution through the "$2.518 \bullet I^{0.5} - 0.657 \bullet I$" term. As explained earlier, the

[2] UNS numbers are listed in *Metals and Alloys in the Unified Numbering System*, published by the Society of Automotive Engineers (SAE International) and co-sponsored by ASTM International.

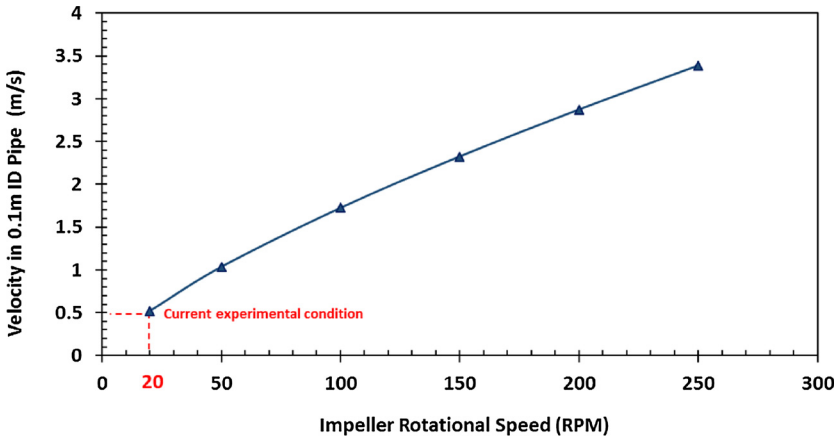

Fig. 3. The relation between impeller rotational speed in the glass cell and velocity of the fluid in single-phase flow through a 0.1 m ID pipe obtained by matching mass transfer rates.

Table 2
Experimental conditions for corrosion studies.

Parameter	Description	
Specimen Characteristics	UNS G10180 with ferritic-pearlitic structure, Flat square geometry with a surface area of 1.5 cm^2	
Temperature	80 °C	
pCO_2	0.53 bar	
pH	**Baseline (without Ca^{2+})**	**With Ca^{2+}**
	6.2 (adjusted with $NaHCO_3$)	6.2 (autogenous in presence of excess amount of $CaCO_3$ reagent)
Electrolyte	1 wt.% NaCl + $NaHCO_3$ (Ionic Strength ~ 0.18 M)	1 wt.% NaCl + $CaCO_3$ (Ionic Strength ~ 0.18 M)
Calcium carbonates saturation (S_{CaCO_3})	0 (without Ca^{2+})	Unity (Ca^{2+} ~ 160 ppm)
Iron carbonates saturation (S_{FeCO_3})	$4 < S_{FeCO_3} < 14$	
Dissolved O_2	< 5 ppb	
Reference Electrode	Saturated Ag/AgCl	
Impeller rotation speed	20 rpm	
Mass Transfer Conditions	Equivalent to 0.5 m/s in a 0.1 m ID pipe	
Electrochemical Techniques	LPR: potential range (± 5 mV vs. OCP), scan rate (0.125 mV/s), B[a] (26 mV) EIS: Frequency range (5000-0.01 Hz), DC voltage (zero vs. OCP), peak to peak amplitude (10 mV), sampling rate (8 points/decade)	
Surface Analysis Techniques	XRD, SEM/EDS, Profilometry	
Test Duration	7 days	

[a] The B value used in the Stern-Geary equation for corrosion rate calculation.

Table 3
Chemical composition of specimens, UNS G10180.

Element	Al	C	Cu	Cr	Mn	Mo	Ni	P	S	Si	Fe
wt.%	0.008	0.18	0.18	0.12	0.75	0.02	0.065	0.011	0.021	0.016	Balance

$CaCO_3$ saturation degree (S_{CaCO_3}) was unity for the experiment with the presence of Ca^{2+}. For more information about the solubility of $FeCO_3$ and/or $CaCO_3$ and calculation of ionic strength, please refer to a recent paper by the authors [8]. The polarization resistance measurements obtained by LPR included solution resistance. Electrochemical impedance spectroscopy (EIS) was used to measure the solution resistance and the polarization resistance at the metal/solution interface was compensated (solution resistance for experiments with and without $CaCO_3$ was 8.3 ± 0.2 Ω·cm^2). The corrected polarization resistance, R_p, was used to calculate the current density (i_{corr}) by employing the Stern-Geary equation [34]:

$$i_{corr} = \frac{B}{R_p} \tag{8}$$

In this study, a B value of 26 mV was used in the Stern-Geary equation to convert the experimental polarization resistance to corrosion rate. This value is commonly accepted in CO_2 environments but is not based on any specific Tafel slopes since the corrosion mechanism is not strictly charge transfer controlled. Instead, this B value was determined by best fit comparison between current densities and weight loss measurements [35–37]. It is understood that the value selected may be dependent on the specific testing conditions and may even change slightly during the tests duration. However, LPR data are here used for trends rather than for obtaining values of corrosion rates which are measured more accurately by WL method. Consequently, the approach adopted in this study was to select a reasonable B value and to keep it constant for all test conditions.

The average corrosion rate by WL method was calculated using Eq. (9):

$$CR = 87.6\frac{W}{DAt} \tag{9}$$

where CR is the corrosion rate reported in mm/y, W is the mass loss in milligram, D is the density of metal in g/cm^3, A is the specimen surface area in cm^2, and t is the exposure time in hours [38].

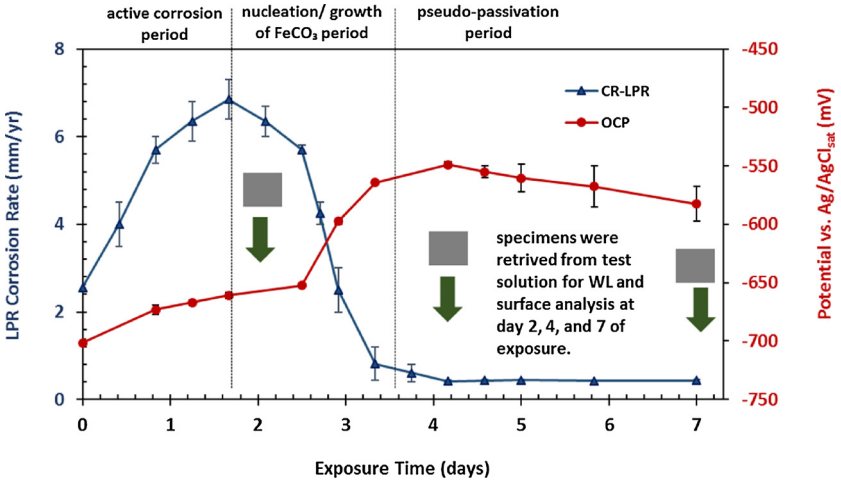

Fig. 4. Change in LPR corrosion rate and open circuit potential with time explained by three different periods: active corrosion, nucleation/growth of $FeCO_3$, and pseudo-passivation (UNS G10180, 80 °C, pCO_2 0.53 bar, pH 6.2, NaCl 1 wt%, $4 < S_{FeCO_3} < 14$, $S_{CaCO_3} = 0$, velocity 0.5 m/s).

3. Results and discussion

In this section, the results of the baseline CO_2 corrosion experiments without Ca^{2+} are presented and discussed. Then, the results of the experiments conducted in $CaCO_3$-saturated electrolyte are presented and compared with the results of baseline experiments.

3.1. Baseline experiments

Fig. 4 shows the corrosion rate obtained by LPR technique and open circuit potential values over the course of experiments without the presence of Ca^{2+} in the electrolyte. The reproducibility of results was indicated by the error bars displayed in Fig. 4, representing the maximum and minimum values from two different experiments (the same is true for other error bars shown in various graphs throughout this manuscript). The corrosion rate trend can be divided into three different periods that correspond to active corrosion, nucleation/growth of $FeCO_3$, and pseudo-passivation. Each period will be discussed separately later on. Fig. 5 shows the comparison of the time-averaged (cumulative) corrosion rate obtained by LPR and WL techniques. There is a reasonable agreement between the corrosion rate obtained by LPR and WL given the error of measurement. Although LPR shows a higher corrosion rate than WL at each measuring point, both methods indicate a decreasing corrosion rate over time.

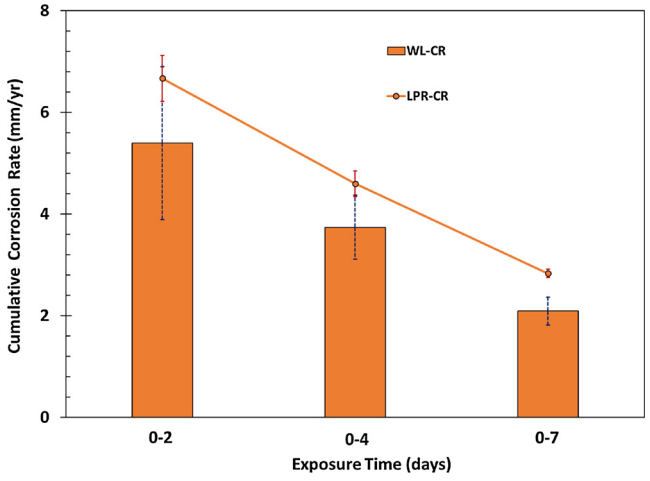

Fig. 5. Time-averaged (cumulative) corrosion rate obtained by LPR and WL techniques (UNS G10180, 80 °C, pCO_2 0.53 bar, pH 6.2, NaCl 1 wt%, $4 < S_{FeCO_3} < 14$, $S_{CaCO_3} = 0$, velocity 0.5 m/s).

3.1.1. Active corrosion period

The increase in the corrosion rate, shown in Fig. 4, in the first two days is characterized as the active corrosion period. In this period, the starting corrosion rate (average) was around 2.5 mm/y and this value reached 6.8 mm/y after 40 h. The increase in corrosion rate is attributed to the ferritic-pearlitic microstructure of UNS G10180 steel. Preferential corrosion of the ferrite (α-Fe) phase over cementite (Fe_3C) phase leaves behind a porous Fe_3C structure on the steel surface. It has been reported that the development of Fe_3C network accelerates the corrosion rate by providing more surface area for cathodic reactions (e.g., hydrogen evolution reaction) within its porous structure leading to a galvanic effect between Fe_3C and α-Fe phase [31,39]. It should be pointed out that while this increase of the corrosion rate as measured by LPR is valid, the actual magnitude of the elevated corrosion rate may be exaggerated by LPR measurements. This is due to the inability of the LPR technique to cope with the galvanic corrosion effect.

At the end of this period, two steel specimens were retrieved from the electrolyte for WL measurements and surface characterization. The top view and cross-section morphology of the surface layers developed in this period are shown in Fig. 6. The porous structure of surface layers is obvious from the cross-section SEM image. The color of the corrosion product layer was gray to black, which is a typical characteristic of Fe_3C residue [40]. The average thickness of the surface layer at this period was around 15 µm. The yellow arrow on the cross-section specimen indicates the calculated metal loss thickness based on WL corrosion rate, which gives a value of 21.3 µm. This value is slightly greater than the measured thickness indicating a possibility that the shear stress created by flow could have removed some of the residual Fe_3C.

3.1.2. Nucleation and growth of $FeCO_3$ period

In the second period, shown in Fig. 4, the corrosion rate continuously decreased from 6.8 mm/y at day 2 to approximately 0.8 mm/y on day 4. At the end of this period, two of the specimens were retrieved from the glass cell for surface analysis and WL measurements. Fig. 6 shows representative SEM images of the top and cross-sectional view of these specimens. The cross-section view revealed that the surface layer adjacent to the steel surface was less porous than previously observed. EDS and XRD confirmed that these layers were made of $FeCO_3$ which precipitated within the Fe_3C structure (EDS and XRD results will be discussed in detail).

$FeCO_3$ can potentially act as a protective layer against corrosion when its precipitation rate is higher than the corrosion rate, measured in the same volumetric units [41]. In the current work, the bulk

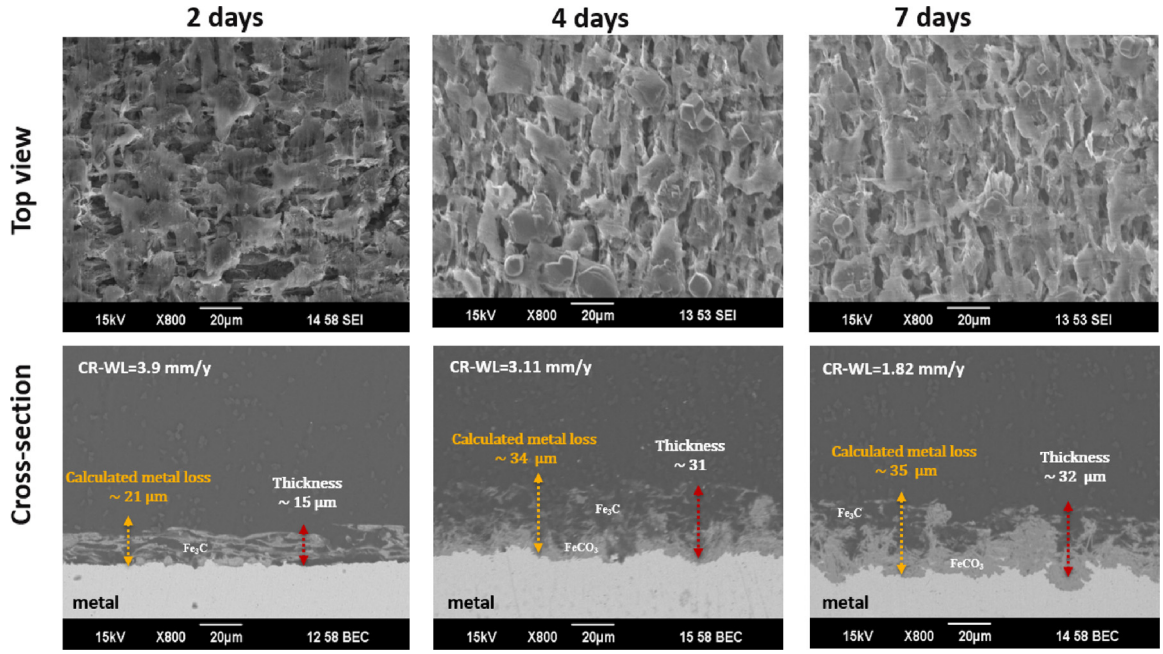

Fig. 6. SEM images of top view and cross-sectional morphology of surface layers exposed to solution in the absence of $CaCO_3$ (note: the CR-WL provided here is specific for the experiment in which the surface characterization is presented here).

saturation degree of $FeCO_3$ was kept between 4 and 14, which would explain why relatively few $FeCO_3$ crystals can be observed in the top view (on the outer edge of the corrosion product layer). However, inside the porous Fe_3C layer, quiescent conditions were achieved and the water chemistry of the solution in contact with the metal surface was significantly different from the bulk solution. The development of Fe_3C layers restricted the transport of corrosion reactants and products through the surface layer. This resulted in a higher pH (due to hydrogen reduction reactions at the metal surface that consumed H^+) and accumulation of Fe^{2+} (generated from corrosion process). Therefore, a significantly higher $FeCO_3$ saturation degree was achieved close to the metal surface. Such local conditions accelerated the precipitation of a relatively protective $FeCO_3$ layer, resulting in a decrease in the corrosion rate and an increase in the corrosion potential over time in this period.

3.1.3. Pseudo-passivation period

Within this manuscript, the term pseudo-passivation refers to a situation when two phenomenon are observed simultaneously: a decrease in corrosion rate along with an increase in corrosion potential due to the formation of iron carbonate at the steel surface [9]. The formation of $FeCO_3$ with low porosity (high density) would have mainly retarded the anodic reaction, which resulted in an increase in OCP [42]. It is assumed that the exposed Fe_3C structure would provide adequate surface area for the cathodic reaction, although, $FeCO_3$ precipitation would have affected this surface area as well. In this period, the corrosion rate was stable, but significantly lower than the corrosion rate in the two previous periods. This was due to further growth of $FeCO_3$ within the other parts of the Fe_3C layers (in addition to the locations close to the steel surface). Consequently, the layer became less porous (denser). It is noteworthy that the thickness of the corrosion product layer was almost the same as observed in the second period. The main reason for this observation was that the corrosion rate in the third period was considerably lower, therefore, the Fe_3C layer could not appreciably be further revealed. Another characteristic of this period is the steep increase in OCP reflected by a decrease in anodic reaction rate due to the precipitation of corrosion product layers on the steel surface. SEM images of the top and cross-section view of the corrosion product layer after 7 days of exposure are shown in Fig. 6. Just like previously discussed for the second period, since the bulk solution was not highly supersaturated with respect to $FeCO_3$, $FeCO_3$ crystals did not form on the outer edge of the Fe_3C layer, as can be seen from top view images in Fig. 6. However, precipitation of $FeCO_3$ adjacent to the steel surface and within the Fe_3C occurred, regardless of the water chemistry in the bulk solution. This is obvious from the cross-section images after 4 days and 7 days of specimen exposure.

In summary, the development of the porous and conductive Fe_3C layer accelerated the corrosion rate in the “active corrosion” period by providing additional cathodic surface area for hydrogen reduction reactions. Then, the Fe_3C layer acted as an anchoring site and facilitated the precipitation of $FeCO_3$ in the second “growth and nucleation of $FeCO_3$” and third “pseudo-passivation” periods. Based on the corrosion rate *versus* time trend and the SEM cross-section images, it seems that there was a critical thickness of Fe_3C layer required for nucleation and subsequent growth of $FeCO_3$ crystals. In the experiments presented above, the cross-section SEM image of specimens at the end of day 2 (active corrosion period) presented a Fe_3C layer 15 µm thick. Therefore, precipitation was likely favored when the thickness of the porous Fe_3C residual was greater than this value. It is fully understood that this critical thickness is highly dependent on a number of operating parameters such as the mass transfer characteristics, the chemistry of the bulk electrolyte, the steel microstructure and composition – consequently, it is only relevant to the experimental conditions of the current research. Fig. 7 shows the corrosion rate measured by WL methods and thickness of Fe_3C at different exposure times. The corrosion rate clearly decreased after 4 days when the Fe_3C layer reached this critical thickness.

The results of EDS analysis (line scan) from the cross-section specimens showed that (close to steel surface) Fe, C, and O elements were present for specimens retrieved at 4 and 7 days of exposure. An example of such EDS analyses for a specimen exposed to the baseline solution for 7 days is illustrated in Fig. 8. The presence of the atomic oxygen in the EDS analysis is consistent with the formation of $FeCO_3$ adjacent to the steel surface and no other compound containing oxygen was expected to form under these experimental conditions. Also, the EDS analysis confirmed the presence of Ni, Cu, Cr, Si, Mn and Mo as residual alloying elements often associated with the presence of the Fe_3C network as shown in Fig. 9, Table (a). These elements are part of the chemical

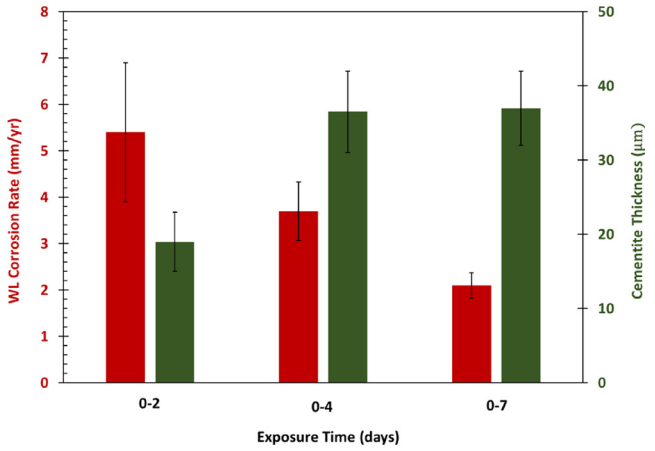

Fig. 7. Corrosion rate by WL and cementite thickness *versus* time in the active (2 days), nucleation/growth of $FeCO_3$ (4 days), and pseudo-passive (7 days) periods.

composition of the UNS G10180 steel. Furthermore, a typical composition of $FeCO_3$ crystal, formed on the top of Fe_3C network, is provided in Table (b), Fig. 9. A trace of Mn was present in such crystals along with Fe, C, and O elements. The presence of a trace amount of Mn, coming from the corroding specimens, in the carbonate crystals is not surprising since $MnCO_3$ (rhodochrosite) shares the same calcite-type crystal structure as $FeCO_3$ and $CaCO_3$, therefore, they can coexist in a carbonate solid solution [43].

XRD data also confirmed the presence of Fe_3C and $FeCO_3$ as the main corrosion products on the steel surface. These XRD patterns from the top view of the corrosion product layers at different exposure times with and without the presence of Ca^{2+} will be discussed and compared in the following section.

3.2. Experiments with $CaCO_3$-saturated solutions

In this part of the paper, the results of $CaCO_3$-saturated corrosion experiments are shown, discussed and compared with the results of the baseline experiments presented above. Figs. 10 and 11 compare the bulk solution pH and $FeCO_3$ saturation degree values over time, respectively. For both series of experiments, these two important parameters were maintained over the course of each experiment. As shown in Fig. 10, the pH values were controlled to pH 6.2 ± 0.1 for both experiments. The initial target value for $FeCO_3$ saturation degree (S_{FeCO_3}) was 10, calculated using Eq. (6); however, it was impossible to maintain this value over the course of experiments since S_{FeCO_3} was affected by the precipitation of $FeCO_3$ after passing the active corrosion periods (initial stages of corrosion process). As indicated in Fig. 11, the average values of S_{FeCO_3} were controlled between 4 and 14 which seems acceptable considering the experimental difficulties. The similarity in water chemistry and test conditions of the baseline and $CaCO_3$-saturated electrolytes facilitates the comparison of corrosion results. This constitutes a considerable improvement from previous studies reported in the literature for which the water chemistry of the experiments was not well controlled rendering any comparisons and conclusions difficult [12,14].

3.2.1. Corrosion rate and open circuit potential with time

The measured corrosion rates obtained by LPR for the experiments conducted in the presence of $CaCO_3$ are compared with that of the baseline experiments in Fig. 12.

The three corrosion periods described earlier for the baseline experiments were also observed in the presence of $CaCO_3$, although several differences could be identified. The kinetics of formation of the protective corrosion product layer was lower in the presence of $CaCO_3$. That may suggest the presence of Ca^{2+} was interfering with the precipitation of $FeCO_3$, slowing the processes of nucleation and/or growth, therefore, a longer active corrosion period was observed in presence of 160 ppm Ca^{2+}. Limited studies in the literature highlight similar findings without proposing any underlying mechanisms: Alsaiari, et al., have reported that calcium ions have an impact on increasing the solubility of $FeCO_3$ and thus decreasing its precipitation rate [44]. According to Fig. 12, regardless of the influence of Ca^{2+} on the earlier periods of the corrosion process, the corrosion rate at the end of the experiment with $CaCO_3$ (pseudo-passivation period) is identical to the baseline experiment in the same corrosion period. This observation suggests that the presence of Ca^{2+} in a solution saturated with $CaCO_3$ would not jeopardize the protectiveness of corrosion product layers when fully developed on the mild steel surface.

For a better understanding of the effect of $CaCO_3$-saturated solution on corrosion rate, Fig. 13 shows a comparison of the cumulative corrosion rate obtained by LPR (line chart) and WL (bar chart) methods at day 2, 4, and 7 of the experiment with and without $CaCO_3$. At each measuring point, LPR shows a higher cumulative corrosion rate compared to WL for both series of experiments. Both LPR and WL techniques indicate that the cumulative corrosion rate in the presence of $CaCO_3$ was lower than the baseline experiment at each measuring point. Another observation is that the difference of cumulative corrosion rate for experiments with and without $CaCO_3$ is decreasing over time, captured by both LPR and WL methods.

The open circuit potential measurements for the two test series are shown in Fig. 14. The overall behavior of OCP with and without $CaCO_3$ was similar, with more positive potentials at the end of the tests as a result of the formation of a relatively dense layer on the metal surface.

3.2.2. Surface layer characterization

Fig. 15 shows the SEM images of top and cross-sectional views of the specimens at different exposure times in the presence of $CaCO_3$. The top view images show the typical morphology of Fe_3C for all specimens. A small quantity of carbonate crystals is present on the top of the developed Fe_3C networks; the presence of such crystals is more obvious after 4 & 7 days of exposure. The cross-sectional images show that the

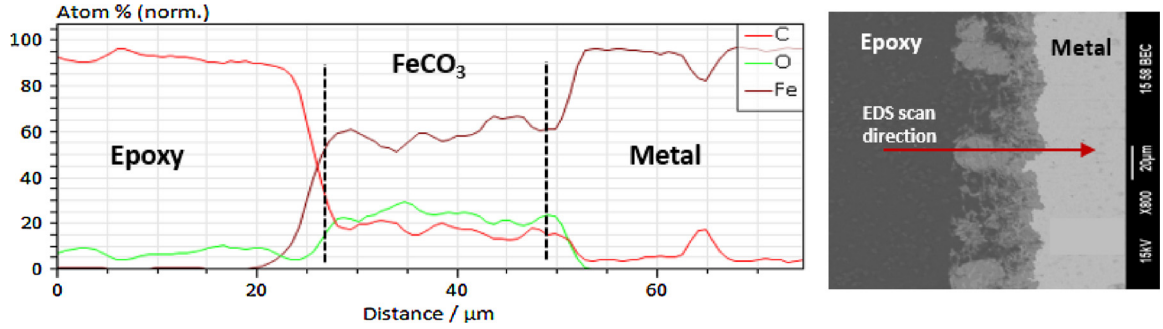

Fig. 8. EDS analysis (line scan) of cross-sectioned corrosion products formed on a specimen exposed to the baseline solution for 7 days.

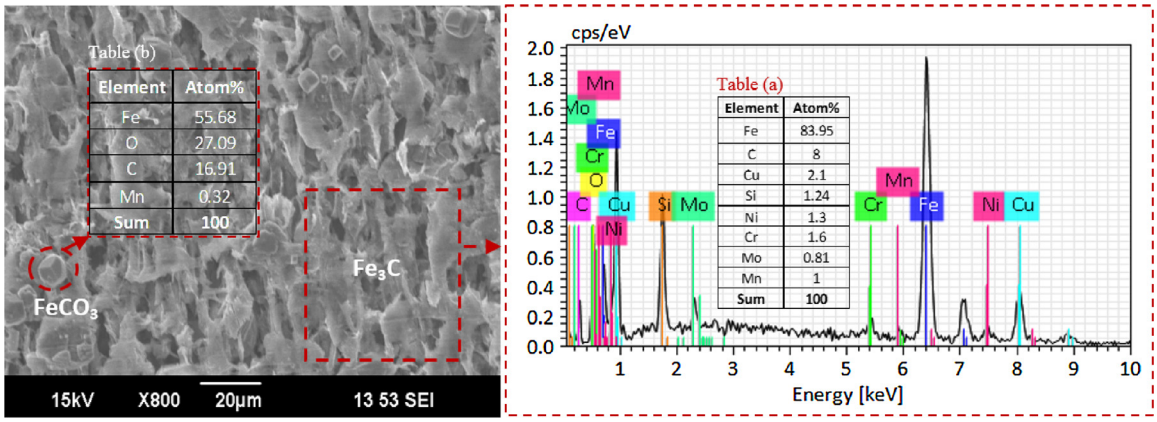

Fig. 9. SEM/EDS analysis (top view) of the corrosion products developed on the surface of UNS G10180 specimens exposed to the baseline solution for 7 days.

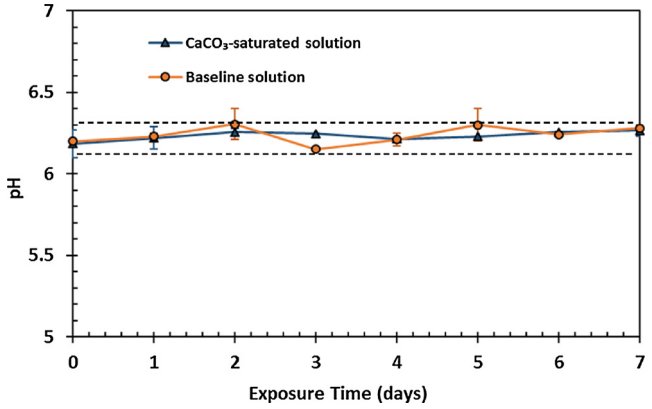

Fig. 10. pH profiles for both baseline and $CaCO_3$-saturated solution over time (pH 6.2 ± 0.1).

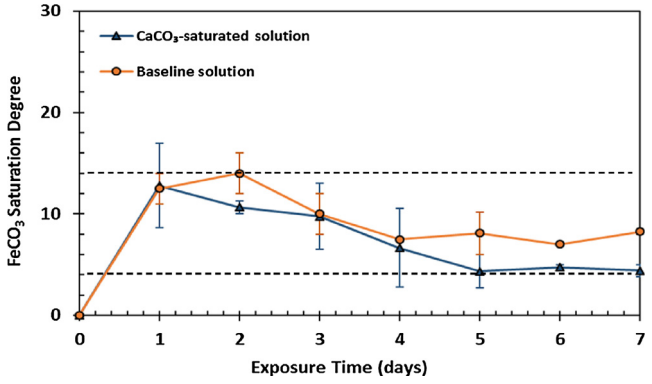

Fig. 11. Variation of $FeCO_3$ saturation degree over time for experiment with and without $CaCO_3$ (the average values of S_{FeCO_3} were controlled between 4 and 14).

surface layer thickness grew steadily up to day 4, at which point its growth was hindered due to the formation of carbonates within the Fe_3C porous structure; this resulted in a rapid decrease in the corrosion rate marking the end of the active corrosion period. The yellow arrows on the cross-sectional images indicate the calculated metal loss thickness, which were obtained from the WL corrosion rate. Similar to the baseline experiments, these calculated values are slightly higher than the measured thickness in the cross-sectional SEM images, suggesting that some of the surface layers may have been removed by flow effect. It is worth mentioning that Fe_3C is fragile and vulnerable to removal by flow [37]. However, precipitation of $FeCO_3$ within the pores of Fe_3C would increase its mechanical strength. The authors believe that the slight difference in the measured and calculated corrosion product thickness could be due to partial removal of Fe_3C in the active corrosion period while the Fe_3C was building up on the steel surface (before precipitation of $FeCO_3$).

The same conclusions related to the baseline experiments on the effect of Fe_3C layers on precipitation of carbonate crystals are also valid for experiments conducted in the presence of $CaCO_3$. In addition, EDS and XRD confirmed the presence of calcium within the carbonate crystals and, to some extent, within the Fe_3C layer. Fig. 16 shows a top view EDS analysis of the corrosion products after 7 days of exposure for an experiment conducted in the presence of $CaCO_3$. Such EDS analysis along with XRD confirmed the formation of solid solutions of iron-calcium carbonate with a trace of manganese (Mn) incorporated into the lattice of such crystals (see Table (a) in Fig. 16). Furthermore, the elemental analysis of the Fe_3C layer in Fig. 16, Table (b), shows residual alloying elements along with Ca are present in the Fe_3C network.

Fig. 17 shows the XRD data obtained for the specimens recovered after different exposure times in $CaCO_3$-saturated electrolytes (solid blue lines) and in electrolytes without $CaCO_3$ (dashed red lines). $FeCO_3$ was the only crystalline phase detected on the steel surface in the absence of Ca^{2+} ions. However, XRD data confirmed that, after 7 days of exposure, a substitutional solid solution of $Fe_xCa_{1-x}CO_3$ was formed in the presence of Ca^{2+} ions. The most intense diffraction, corresponding to the *hkl* (104) Bragg peak, for siderite ($FeCO_3$) and calcite ($CaCO_3$) occurs at 32.07 and 29.42 2θ, respectively (CuK_α radiation). The effect of Ca^{2+} on the corrosion product layers can be seen by comparing the XRD data of experiments with and without $CaCO_3$ at day 4 and 7. The XRD data are almost identical with/without $CaCO_3$ for the first 2 days when the Fe_3C layers are developing. However, $FeCO_3$ peaks for the experiment in the presence of Ca^{2+} are broadened and shifted toward the reference peaks for $CaCO_3$, indicating heterogeneous substitution of Fe by Ca in the lattice of $FeCO_3$. This phenomenon is more obvious for XRD data at day 7 of the experiment which revealed a substitutional solid solution with a formula of $Fe_{0.898}Ca_{0.102}CO_3$, by determining the mole fraction of Ca incorporated into $FeCO_3$ lattice using Bragg's law [11]. Although all of the $FeCO_3$ peaks are slightly shifted towards the left, in the presence of Ca^{2+} ions, the more intense peaks associated with (104) and (116) Miller planes located at 32.07 and 52.7 degrees are more easily recognizable after 7 days of exposure. Another observation is that the intensity of peaks related to α-Fe is decreasing over time for both series of experiments. This indicates that surface layers were increasing in depth and, as a result, incident X-rays could not reach the steel substrate as easily.

Fig. 18 illustrates the EDS line scan analysis (left-hand graph) of a cross-sectioned specimen exposed to $CaCO_3$-saturated solution for 7 days shown by SEM (right-hand image). Such analysis proved a pure $FeCO_3$ layer was formed as an inner layer adjacent to the steel surface. Whereas the outer corrosion product layer was $Fe_xCa_yCO_3$ (x + y = 1)

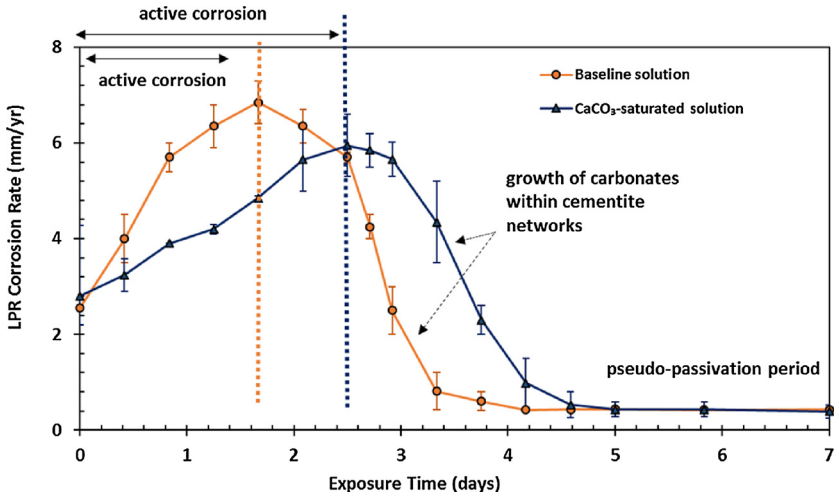

Fig. 12. Comparison of LPR corrosion behavior of UNS G10180 exposed to $CaCO_3$-saturated and baseline ($CaCO_3$-free) aqueous conditions.

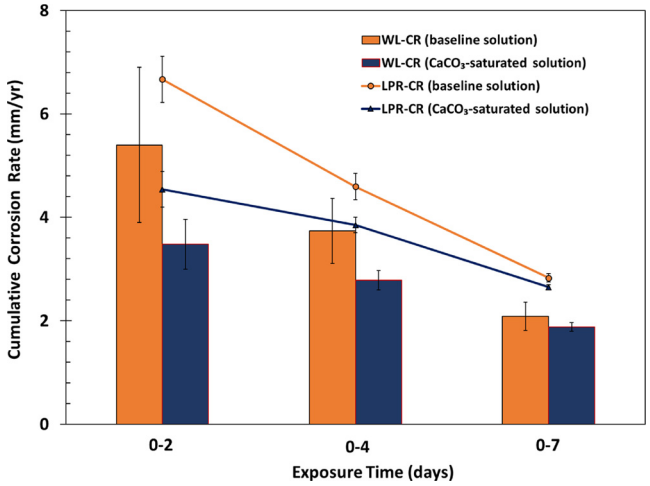

Fig. 13. Comparison of cumulative corrosion rate obtained by LPR and WL methods with and without $CaCO_3$ after 2, 4, and 7 days of exposure.

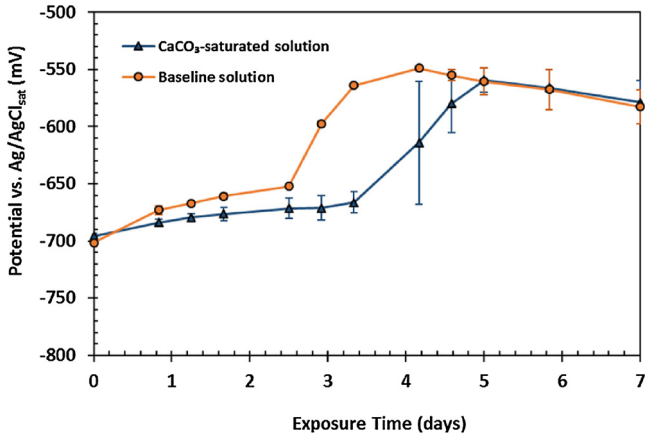

Fig. 14. Comparison of OCP over time for UNS G10180 exposed to solutions with and without $CaCO_3$.

with an atomic percentage of Fe being dominant over Ca within this solid solution (x > y). The EDS results were in accordance with XRD observation in the presence of Ca^{2+}.

The vulnerability of the specimens to localized corrosion was also evaluated in this study. Profilometry of the specimen surfaces was performed after removing corrosion product layers by Clarke solution [45] and no localized corrosion was observed for any of the above experiments with or without $CaCO_3$.

4. Conclusions

The following conclusions are drawn:

- The development of Fe_3C acted as anchoring sites for precipitation of $Fe_xCa_{1-x}CO_3$ and $FeCO_3$ within its porous structure in solutions with and without $CaCO_3$, respectively.
- There existed a critical thickness for the Fe_3C network that favored the precipitation of carbonate crystals due to different water chemistry within the Fe_3C compared to the bulk solution, *i.e.*, higher pH and $FeCO_3$ saturation.
- The formation of substitutional solid solution, $Fe_{0.898}Ca_{0.102}CO_3$, (outer layer) along with $FeCO_3$ (inner layer) retarded the anodic reaction (and the cathodic reaction, to a lesser degree) causing low general corrosion at the end of the exposure with no localized corrosion. There was no difference in this behavior when comparing to what was seen in the experiments without Ca^{2+}, where only $FeCO_3$ precipitated.
- The protectiveness of the corrosion product was not jeopardized in the presence of Ca^{2+} ions when the solution was saturated with respect to $CaCO_3$.
- Overall, in the conducted experiments, CO_2 corrosion mechanisms were not altered in $CaCO_3$ saturated solutions (with Ca^{2+} ~ 160 ppm) after full development of corrosion products (pseudo-passivation period).

Data availability

The raw data required to reproduce the findings within this manuscript are available upon the interest of the readers. Please contact Hamed Mansoori (hm419213@ohio.edu).

Acknowledgments

The authors would like to thank the following companies for their financial support: Anadarko, Baker Hughes, BP, Chevron, CNOOC, ConocoPhillips, DNV GL, ExxonMobil, M-I SWACO (Schlumberger), Multi-Chem (Halliburton), Occidental Oil Company, PTT, Saudi Aramco, Shell Global Solutions, SINOPEC (China Petroleum), TransCanada, TOTAL, and Wood Group Kenny.

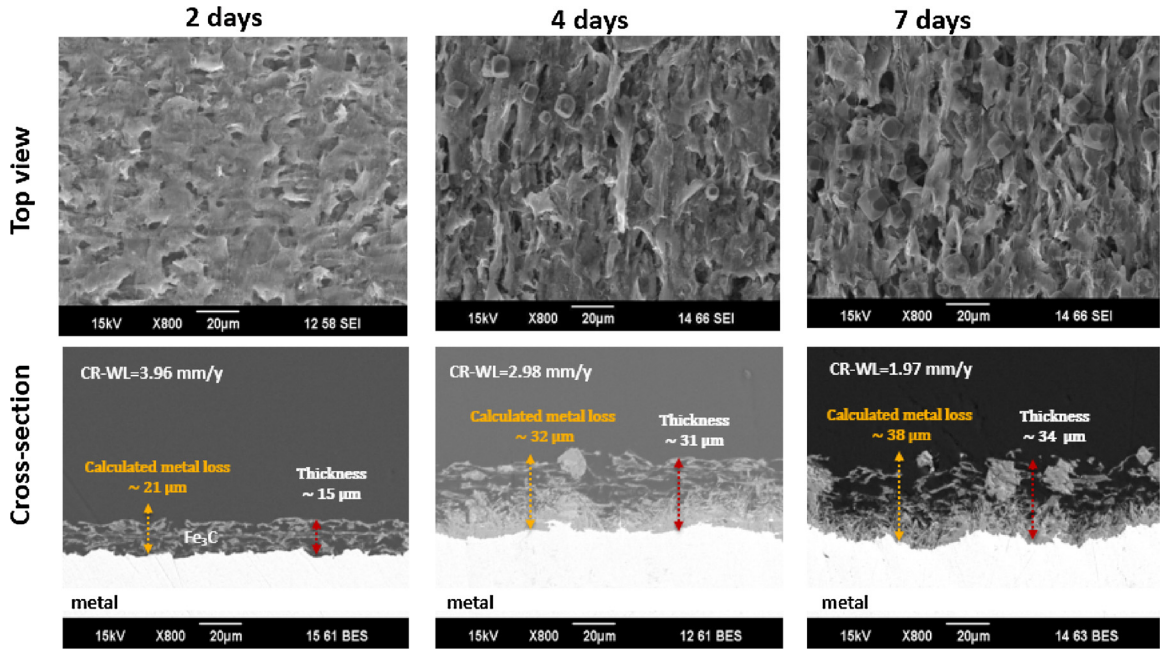

Fig. 15. Top and cross-sectional views of specimens retrieved from the test condition with $CaCO_3$ present after 2, 4 and 7 days of exposure.

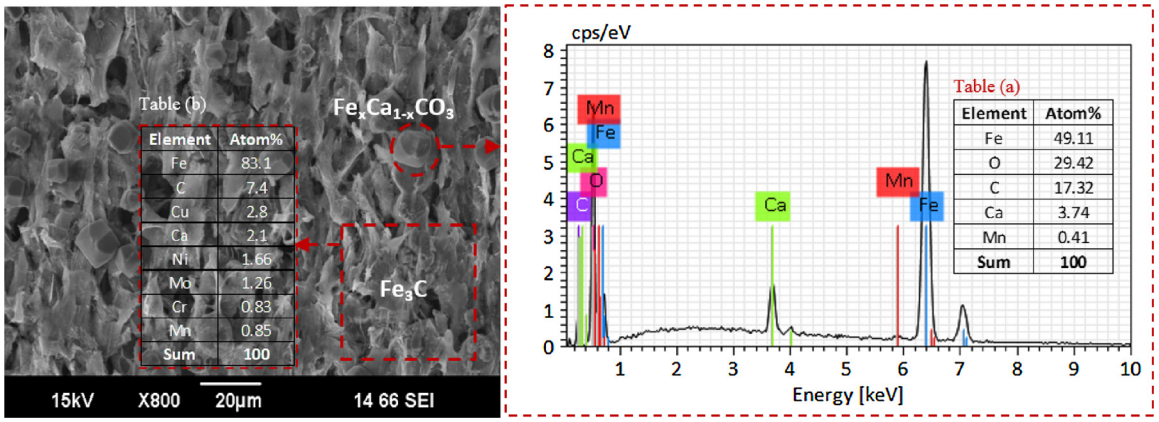

Fig. 16. SEM/EDS analysis (top view) of the surface layers on UNS G10180 developed from a solution saturated with $CaCO_3$ after 7 days of exposure.

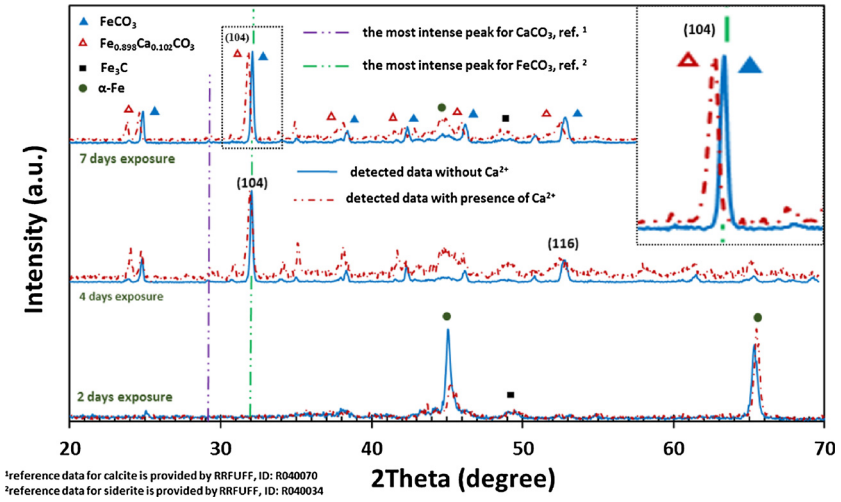

Fig. 17. XRD patterns of surface layers detected on the steel surface after 2, 4, and 7 days of exposure with/without the presence of Ca^{2+}.

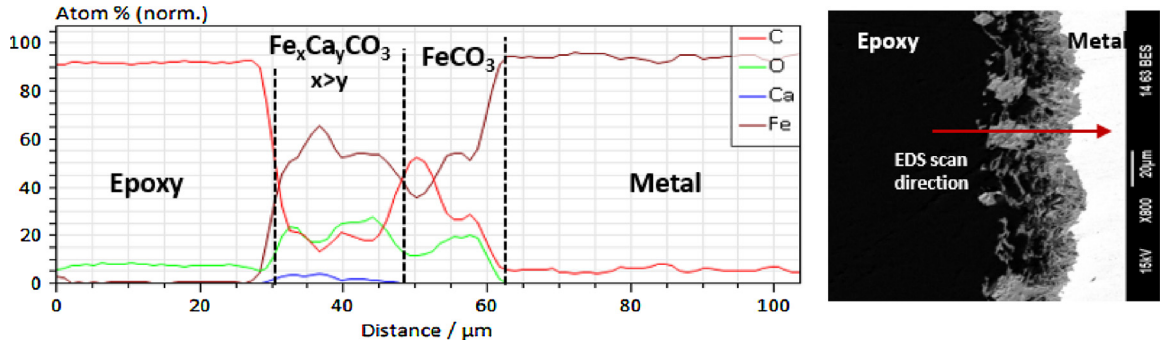

Fig. 18. Elemental analysis (line scan) of cross-sectioned corrosion products formed on a specimen exposed to $CaCO_3$-saturated solution for 7 days.

References

[1] H. Mansoori, R. Mirzaee, F. Esmaeilzadeh, A. Vojood, A. Soltan Dowrani, Pitting corrosion failure analysis of a wet gas pipeline, Eng. Fail. Anal. 82 (2017) 16–25.

[2] J.E. Oddo, M.B. Tomson, others, Why scale forms in the oil field and methods to predict it, SPE Prod. Facil. 9 (1994) 47–54.

[3] A. Antony, J.H. Low, S. Gray, A.E. Childress, P. Le-Clech, G. Leslie, Scale formation and control in high pressure membrane water treatment systems: a review, J. Membr. Sci. 383 (2011) 1–16.

[4] H. Mansoori, F. Esmaeilzahed, D. Mowla, A.H. Mohammadi, Case study: production benefits from increasing C-values, Oil Gas J. 111 (2013) 64–73.

[5] W.A. House, J.A. Tutton, An investigation of the heterogeneous nucleation of calcite, J. Cryst. Growth 56 (1982) 699–710.

[6] H. Mansoori, R. Mirzaee, A.H. Mohammadi, F. Esmaeelzadeh, Acid washes, oxygenate scavengers work against gas gathering failures, Oil Gas J. 111 (2013) 106–111.

[7] H. Mansoori, R. Mirzaee, A.H. Mohammadi, Pitting Corrosion Failures of Natural Gas Transmission Pipelines, IPTC, 2013.

[8] H. Mansoori, D. Young, B. Brown, M. Singer, Influence of calcium and magnesium ions on CO_2 corrosion of carbon steel in oil and gas production systems-a review, J. Nat. Gas Sci. Eng. 59 (2018) 287–296.

[9] J. Han, S. Nesic, Y. Yang, B. Brown, Spontaneous passivation observations during scale formation on mild steel in CO_2 brines, Electrochim. Acta 56 (2011) 5396–5404.

[10] P.E. Dresel, A.W. Rose, Chemistry and Origin of Oil and Gas Well Brines in Western Pennsylvania, The Pennsylvania State University, 2010 Open-File Report OFOG 10–01.0.

[11] S.N. Esmaeely, D. Young, B. Brown, S. Nesic, Effect of incorporation of calcium into iron carbonate protective layers in CO_2 corrosion of mild steel, Corrosion 73 (2016) 238–246.

[12] S.N. Esmaeely, Y.-S. Choi, D. Young, S. Nesic, Effect of calcium on the formation and protectiveness of iron carbonate layer in CO_2 corrosion, Corrosion 69 (2013) 912–920.

[13] C. Ding, K. Gao, C. Chen, Effect of Ca^{2+} on CO_2 corrosion properties of X65 pipeline steel, Int. J. Miner. Metall. Mater. 16 (2009) 661–666.

[14] L.M. Tavares, E.M. da Costa, J.J. de O. Andrade, R. Hubler, B. Huet, Effect of calcium carbonate on low carbon steel corrosion behavior in saline CO_2 high pressure environments, Appl. Surf. Sci. 359 (2015) 143–152.

[15] E. Eriksrud, T. Sontvedt, Effect of flow on CO_2 corrosion rates in real and synthetic formation waters, Proc. Symp. CO_2 Corros. Oil Gas Ind. NACE International 1 (1984) 20–38.

[16] Y. Hua, A. Shamsa, R. Barker, A. Neville, Protectiveness, morphology and composition of corrosion products formed on carbon steel in the presence of Cl^-, Ca^{2+} and Mg^{2+} in high pressure CO_2 environments, Appl. Surf. Sci. 455 (2018) 667–682.

[17] X. Jiang, Y.G. Zheng, D.R. Qu, W. Ke, Effect of calcium ions on pitting corrosion and inhibition performance in CO_2 corrosion of N80 steel, Corros. Sci. 48 (2006) 3091–3108.

[18] Y. Zhang, H. Shaw, R. Farquhar, R. Dawe, The kinetics of carbonate scaling-application for the prediction of downhole carbonate scaling, J. Pet. Sci. Eng. 29 (2001) 85–95.

[19] T.H. Chong, R. Sheikholeslami, Thermodynamics and kinetics for mixed calcium carbonate and calcium sulfate precipitation, Chem. Eng. Sci. 56 (2001) 5391–5400.

[20] N. Spanos, P.G. Koutsoukos, Kinetics of precipitation of calcium carbonate in alkaline pH at constant supersaturation. Spontaneous and seeded growth, J. Phys. Chem. B 102 (1998) 6679–6684.

[21] G.X. Zhao, L. Jian-Ping, H. Shi-Ming, L.U. Xiang-Hong, Effect of Ca^{2+} and Mg^{2+} on CO_2 corrosion behavior of tube steel, J. Iron Steel Res. Int. 12 (2005) 38–42.

[22] K.S. Pitzer, Ion interaction approach: theory and data correlation, Act. Coeff. Electrolyte Solut. (1991) 75–154.

[23] S. Nesic, Effects of multiphase flow on internal CO_2 corrosion of mild steel pipelines, Energy Fuels 26 (Jul) (2012) 4098–4111.

[24] ASTM G31-72, Guide for Laboratory Immersion Corrosion Testing of Metals, ASTM International, 2004.

[25] W.B. Fortune, M.G. Mellon, Determination of iron with o-phenanthroline: a spectrophotometric study, Ind. Eng. Chem. Anal. Ed. 10 (1938) 60–64.

[26] X. Zhong, B. Brown, W. Li, S. Nesic, M. Singer, How to maintain a stable solution chemistry when simulating CO_2 corrosion in a small volume laboratory system, NACE International, Paper No. 7780, (2016).

[27] D.C. Silverman, The rotating cylinder electrode for examining velocity-sensitive corrosion—a review, Corrosion 60 (Nov) (2004) 1003–1023.

[28] H. Saraç, M.A. Patrick, A.A. Wragg, Physical properties of the ternary electrolyte potassium ferri-ferrocyanide in aqueous sodium hydroxide solution in the range 10–90 C, J. Appl. Electrochem. 23 (1993) 51–55.

[29] F.P. Berger, F.-L. Hau, Mass transfer in turbulent pipe flow measured by the electrochemical method, Int. J. Heat Mass Transf. 20 (Nov) (1977) 1185–1194.

[30] Z. Ma, Y. Yang, B. Brown, S. Nesic, M. Singer, Investigation of precipitation kinetics of FeCO3 by EQCM, Corros. Sci. 141 (Aug) (2018) 195–202.

[31] S. Ieamsupapong, B. Brown, M. Singer, S. Nesic, Effect of solution pH on corrosion product layer formation in a controlled water chemistry system, NACE International, Paper No. 9160, (2017).

[32] S. Nesic, Carbon dioxide corrosion of mild steel, Uhlig's Corrosion Handbook vol. 51, John Wiley & Sons, 2011, pp. 229–245.

[33] W. Sun, S. Nesic, R.C. Woollam, The Effect of Temperature and Ionic Strength on Iron Carbonate ($FeCO_3$) Solubility Limit, Corros. Sci. 51 (2009) 1273–1276.

[34] M. Stern, A.L. Geary, Electrochemical Polarization I. A Theoretical Analysis of the Shape of Polarization Curves, J. Electrochem. Soc. 104 (1957) 56–63.

[35] Y. Yang, B. Brown, S. Nesic, M.E. Gennaro, B. Molinas, Mechanical Strength And Removal Of A Protective Iron Carbonate Layer Formed On Mild Steel In CO_2 corrosion, NACE International, Paper No. 10383, (2010).

[36] F. Madani Sani, B. Brown, Z. Belarbi, S. Nesic, An experimental investigation on the effect of Salt concentration on uniform CO_2 corrosion, NACE International, Paper No.13026, (2019).

[37] M. Di Bonaventura, B. Brown, M. Singer, S. Nesic, Effect of flow and steel microstructure on the formation of iron carbonate, NACE International, Paper No. 11179, (2018).

[38] M.G. Fontana, Corrosion Engineering, 3rd edition, McGraw-Hill Book Company, New York, 1985.

[39] F. Farelas, B. Brown, S. Nesic, others, Iron carbide and its influence on the formation of protective iron carbonate in CO_2 corrosion of mild steel, NACE International, Paper No. 2291, (2013).

[40] K. Videm, The influence of pH and concentration of bicarbonate and ferrous ions on the CO_2 corrosion of carbon steels, NACE International, Paper No. 83, (1993).

[41] S. Nesic, Key issues related to modelling of internal corrosion of oil and gas pipelines – a review, Corros. Sci. 49 (2007) 4308–4338.

[42] J.M. Olivo, B. Brown, S. Nesic, others, Modeling of corrosion mechanisms in the presence of quaternary ammonium chloride and imidazoline corrosion inhibitors, NACE International, Paper No. 7406, (2016).

[43] T. Zoltai, J.H. Stout, Mineralogy: Concepts and Principles, Burgess Pub. Co., 1984.

[44] H.A. Alsaiari, A. Kan, M. Tomson, others, Effect of calcium and Iron (II) ions on the precipitation of calcium carbonate and ferrous carbonate, SPE J. 15 (2010) 294–300.

[45] ASTM G1, Standard Practice for Preparing, Cleaning, and Evaluating Corrosion Test, ASTM International, 2011.